RSC Advances

PAPER

View Article Online
View Journal | View Issue

Open Access Article. Published on 10 January 2025. Downloaded on 1/22/2026 12:59:05 AM.
This article is licensed under a Creative Commons Attribution-NonCommercial 3.0 Unported Licence.

Check for updates

Cite this: *RSC Adv.*, 2025, **15**, 795

Enhanced performance of UiO-66 for supercapacitor applications through oxidation *via* the Hummers' method

Dina Okba,[ad] Sameh Hassan,*[b] Abdel Aleem H. Abdel Aleem,[d] Mohamed T. Shehab El-din,[a] Ibrahim El Tantawy El Sayed[d] and Ahmed S. Abou-Elyazed*[cd]

Received 31st October 2024
Accepted 25th December 2024

DOI: 10.1039/d4ra07779b

rsc.li/rsc-advances

Supercapacitors (SCs) are gaining attention in energy storage due to their high-power density, rapid charge/discharge ability, and long life cycle. Improving these features relies on developing advanced electrode materials with better energy storage properties. This study explores UiO-66, a zirconium-based metal–organic framework (MOF), which offers advantages like a large surface area, tunable pore sizes, and stability. However, its poor electrical conductivity limits its use in supercapacitors. Herein, we applied the Hummers' method to oxidize UiO-66, creating an oxidized form, H-UiO-66, with enhanced conductivity. This material was characterized by various techniques, including SEM-EDX, XRD, XPS, FTIR, and BET analysis, while electrochemical tests (GCD, CV, and EIS) confirmed a significant improvement in specific capacitance—82.8 F g^{-1} for H-UiO-66 *versus* 0.18 F g^{-1} for pristine UiO-66 at 1 mA. These improvements stem from increased conductivity and electrochemical activity due to UiO-66 graphitization, highlighting the Hummers' method's effectiveness in transforming UiO-66 into a viable supercapacitor material.

1 Introduction

Supercapacitors (SCs), often referred to as ultracapacitors or electrochemical capacitors, have attracted considerable interest as energy storage solutions because of their impressive power density, swift charge and discharge capabilities, and extended cycle longevity. These devices bridge the gap between traditional capacitors and batteries, offering a unique combination of high energy and power capabilities. To enhance their performance, extensive research has focused on developing new electrode materials with improved energy storage characteristics. One promising material that has emerged in recent years is UiO-66, a metal–organic framework (MOF). UiO-66, derived from the University of Oslo acronym UiO (Universitetet i Oslo), is a zirconium-based MOF featuring a three-dimensional porous structure. It is composed of $Zr_6O_4(OH)_4$ secondary building units connected by carboxylate linkers, resulting in a highly stable and crystalline framework. UiO-66's large surface area, adjustable pore size, and exceptional stability make it an ideal candidate for applications like gas storage, catalysis, and energy storage devices, including supercapacitors.

In the context of supercapacitors, UiO-66 offers several advantageous properties that contribute to improved energy storage performance. Firstly, its large surface area provides numerous active sites for charge storage. Effective electrolyte penetration is made possible by the porous structure, facilitating ion diffusion and improving the electrochemical performance of the supercapacitor. Additionally, the chemical stability of UiO-66 ensures long-term cycling stability, minimizing capacity degradation and enabling extended device lifetimes. Nonetheless, the weak UiO-66 electrical conductivity minimizes its use to be an energy storage substance. Enhancing the UiO-66 electrical conductivity is essential for improving its electrochemical efficiency and storage of energy capabilities.[1,2]

To harness the potential of UiO-66 in supercapacitor applications, researchers have explored various strategies to incorporate it into electrode materials. One approach involves the synthesis of UiO-66 nanoparticles and their subsequent integration into conductive matrices, such as carbon nanotubes, graphene, or conducting polymers. Utilizing conductive polymers is the typical approach to improve the electrical conductivity of UiO-66.[3–5] However, the integration of two materials could lead to issues regarding their compatibility. To prevent this from occurring, closely following the production UiO-66 process is anticipated to improve the storage energy capacity while avoiding compatibility challenges,[6,7] for

[a]*Central Laboratory of Aquaculture Research, (CLER), Agricultural Research Center, Sharqia, Egypt*
[b]*Physics Department, Faculty of Science, Menoufia University, Shebin El-Koom, 13829, Egypt. E-mail: sameh.hassan@science.menofia.edu.eg*
[c]*Institute of Intelligent Manufacturing Technology, Shenzhen Polytechnic University, Shenzhen, 518055, P. R. China. E-mail: ahmedphysical90@gmail.com*
[d]*Chemistry Department, Faculty of Science, Menoufia University, Shebin El-Koom, 13829, Egypt*

Open Access Article. Published on 10 January 2025. Downloaded on 1/22/2026 12:59:05 AM.
This article is licensed under a Creative Commons Attribution-NonCommercial 3.0 Unported Licence.

example, the development of amorphous UiO-66,[6] altering synthesized temperature, mixing speeds,[8] and design bimetallic Zn/Zr UiO-66.[7] The post-treatment has also been implemented to improve the electrochemical effectiveness of MOFs[1,9–13] Graphene has been recognized as one of the most effective materials for SCs because of its behavior as a double-layer capacitor. Nonetheless, there exists an insufficient study examining the UiO-66 graphitization for using electroactive substances for SCs.

In this study, the Hummers' method as a promising and facile technique for the development of sorbent materials, such as metal–organic frameworks (MOFs), is being explored for its potential to improve the physicochemical properties of the developed structure of UiO-66 far from the high cost pyrolysis methods. These properties are characterized by measuring the electrochemical behaviors such as charge/discharge galvanostatic (CDG), cyclic voltammetry (CV), electrochemical impedance spectroscopy (EIS), and the crystallinity check through XRD, surface morphology by SEM, and chemical characterization by XPS, FTIR, and BET. This three-dimensional net-like structure of atoms provides a variety of binding, catalytic, and temporary storage sites, establishing it as a promising candidate for supercapacitor applications.

2 Experimental section

2.1. Materials

All materials utilized in this research were of analytically high purity levels and were employed without additional purification. Among the primary chemicals utilized in the study, zirconyl chloride octahydrate ($ZrOCl_2 \cdot 8H_2O$), and 1,4-benzene dicarboxylic acid (BDC), were purchased from Sigma Aldrich. Sodium nitrate, sulfuric acid (H_2SO_4, 98%), potassium permanganate ($KMnO_4$), 304-stainless steel, *N*-dimethylpyrrolidone (NMP), polyvinylidene fluoride (PVDF) and sodium sulfate anhydrous (Na_2SO_4, 99%) were purchased from Himedia, India.

2.2. Synthesis of UiO-66(Zr)

To synthesize UiO-66(Zr), (969 mg, 1.5 mmol) of $ZrOCl_2 \cdot 8H_2O$ and (500 mg, 1.5 mmol) of BDC were combined and ground together at room temperature for 10 min. The resulting mixture was then transferred to the Teflon lined autoclave and heated at 130 °C for 12 h. After cooling to room temperature, the obtained white solid was washed with ethanol at 70 °C for 3 h and subsequently dried under vacuum at 150 °C for 12 h.[14]

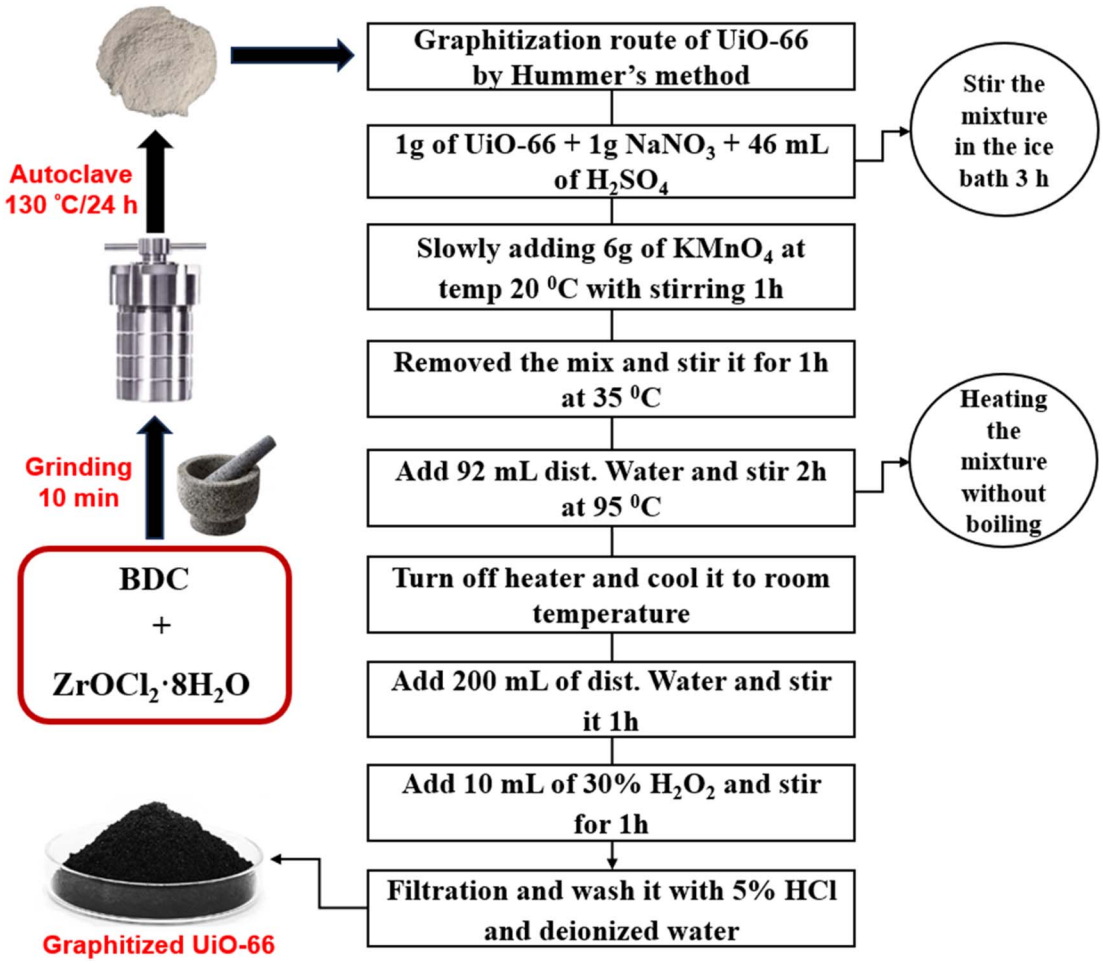

Fig. 1 Schematic description for the preparation of UiO-66 and graphitization by Hummer's method.

 © 2025 The Author(s). Published by the Royal Society of Chemistry

Open Access Article. Published on 10 January 2025. Downloaded on 1/22/2026 12:59:05 AM.
This article is licensed under a Creative Commons Attribution-NonCommercial 3.0 Unported Licence.

2.3. Application of Hummers' method on UiO-66(Zr) as graphene oxide preparation method

A UiO-66 was oxidized following Hummers' method.[15] 1 g of UiO-66 was dispersed in 46 mL of sulfuric acid, and 1 g of sodium nitrate was added, additionally, 6 g of $KMnO_4$, and the mixture was stirred continuously. The mixture's color changed from white to dark brown, accompanied by a slightly exothermic reaction. To control the temperature at around 35 °C, the reaction vessel was placed in an ice bath and left for 1 h for extended oxidation. Next, 92 mL of distilled water was added, and the mixture was stirred at 95 °C for 2 h. The reaction mixture turned reddish-brown and was quenched with H_2O_2. It was then washed several times with 5% HCl and distilled water. The final product is referred to as H-UiO-66 as represented in Fig. 1.

2.4. Electrode preparation

The synthesized H-UiO-66 served as an active component, mixed with graphite and PVDF, with mass fractions of 80%, 10%, and 10%, respectively. The resulting mixture was carefully dispersed in absolute *N*-methyl-2-pyrolidone and then drop-casting onto a piece of stainless steel (0.3 mm thick, 1 cm^2 area, and 95% purity), which served as the current collector. The active material exhibited a mass loading of 7.1 mg cm^{-2}. The prepared electrode was later dried at 70 °C in the oven for 2 h to eliminate the solvent.

2.5. Characterization

Nitrogen sorption at −196 °C was performed using a 3H-2000PS1 system after degassing samples at 150 °C for 2 h under vacuum (1×10^{-3} torr). XRD patterns were recorded with a Philips PW 3710/31 X-ray generator (Philips, Japan). XRD patterns were recorded using a Rigaku D/Max-2550 diffractometer (Cu Kα, $\lambda = 1.542$ Å) with a SolX Detector, scanning at $2\theta = 5°–50°$. SEM images were captured on a SUPRA 55 with a 20 kV acceleration voltage. FTIR was obtained using the method of KBr disc with a Nexus 870 spectrometer of FTIR from Thermo Fisher Scientific, USA. XPS analysis was performed utilizing (PerkinElmer 5600, USA) which featured a beam diameter of X-ray of 0.8 mm, with the area for analysis measuring 1 mm. Samples, which were deposited on indium sheets, underwent irradiation with a 200 W Mg Kα (Al Kα) radiation source. On a Shimadzu TA-50, thermal analysis (TGA) was performed under a nitrogen atmosphere with a heating rate of 10 °C min^{-1}. The Potentiostat (SP-150) was applied to evaluate the electrochemical characteristics of the composite samples within a 3-electrode configuration utilizing Na_2SO_4 as the electrolyte, the Ag/AgCl electrode (KCl Sat.) is the electrode of reference, and the platinum wire electrode is the counter electrode.

3 Results and discussion

3.1. Characterization of materials

The UiO-66 and synthesized H-UiO-66 samples underwent analysis through XRD to investigate structural alterations prior to and following treatments, particularly the interlayer distances. The UiO-66 pattern reflects the typical structure with strong peaks around $2\theta = 7.4°$, 8.5°, 14.8° and 25.8°, confirming the successful synthesis of UiO-66 (Fig. 2).[16] Upon graphitization *via* Hummers' method, represented by the H-UiO-66, the XRD pattern changes, indicating the graphitization of the UiO-66 framework. The broadening of peaks, particularly at lower angles (below 10°), suggests the maintenance of the Zr-cluster with some loss of crystallinity or an increased disorder due to the presence of the graphitic material. Additionally, the presence of new peaks, especially near $2\theta = 15.9°$, is indicative of graphitic structures formed during the process and the acquiring of the hydrophilic oxygen-containing that increased the *d*-spacing between interatomic layers.[17] The XRD results indicated that the enhanced electrical conductivity of UiO-66 is likely due to the presence of graphene-like sheets within its matrix. Additionally, peaks at 37.3°, 39.6°, and 41.6° confirmed the presence of MnO_2 in the structure, originating from the permanganate source.[18]

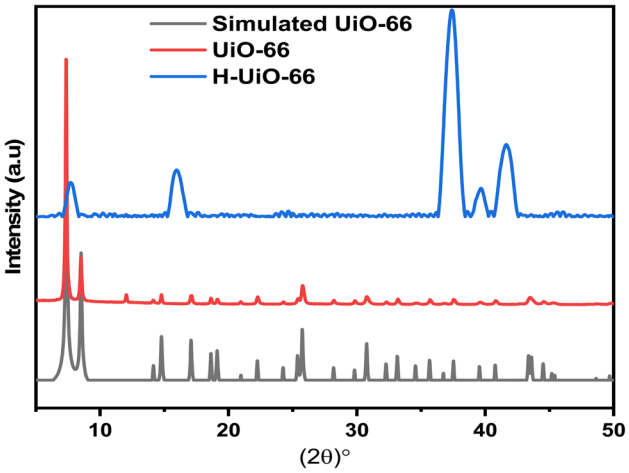

Fig. 2 XRD patterns for various samples.

The chemical transition of the H-UiO-66 and UiO-66 was additionally validated through infrared (FTIR) spectroscopy, and the outcomes are outlined in Fig. 3 for each of the two samples. Both H-UiO-66 and UiO-66 have bands at 3420 cm^{-1} attributed to the presence of hydroxyl groups and adsorbed water. In the case of UiO-66, distinct peaks were observed, with the symmetric vibration peak of O–Zr–O at 746 cm^{-1} and another at 664 cm^{-1} corresponding to the symmetric vibration peak of O–Zr–O.[19,20] The peaks at 1580 cm^{-1} and 1400 cm^{-1} align with the symmetrical stretching vibrations of the C=O bond in the –COO group within UiO-66. The spectrum of FTIR of H-UiO-66 displays an observed peak above 3000 cm^{-1}, which displays the –OH stretching of the group of COOH while the centered bond at 2933 cm^{-1} is attributed to the stretching of C–H. Also, the observed peaks at 1140 cm^{-1} and 1050 cm^{-1} are attributed to the bond of Zr–O stretching vibration. While the peaks at 665 cm^{-1} and 471 cm^{-1} sequentially signify the Zr–OH and Zr–O bonds stretching vibration within the 12 units of UiO-66 skeleton denoted as $Zr_6O_4(OH)_4(COO)_6$.[21,22]

The characteristic absorption peaks of UiO-66 at 1140 cm^{-1} and 1050 cm^{-1} are evident in the complex's infrared spectrum.

Open Access Article. Published on 10 January 2025. Downloaded on 1/22/2026 12:59:05 AM.
This article is licensed under a Creative Commons Attribution-NonCommercial 3.0 Unported Licence.

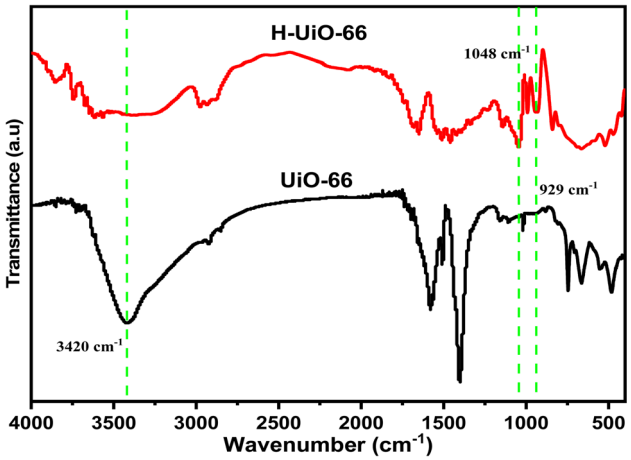

Fig. 3 FT-IR spectra of UiO-66 and H-UiO-66 synthesized materials.

Furthermore, the stretching vibration of C–O (alkoxy) is manifested at 1048 cm^{-1}, and the peak corresponding to epoxy or peroxide groups is observed at 929 cm^{-1},[23] indicating the oxidation of the organic linker of UiO-66 network. Additionally, the characteristic peaks observed at 521 cm^{-1} and 427 cm^{-1} could be attributed to Mn–O bonds from the permanganate reduction. The infrared spectrum of the compound closely resembled that of MnO_2.

Fig. 4 shows the SEM images used to determine the particle size and morphology of UiO-66 and H-UiO-66, as well as to examine the surface of each composite, confirming the successful preparation of H-UiO-66. The synthesized UiO-66 was displayed with a flakelike shape surface morphology, covered with a fluff layer as shown in Fig. 4a. Fig. 4b displayed the results obtained from SEM of H-UiO-66, revealing a cobweb shape covered by grown fibre shape of MnO_2 as reported previously in the literature.[24,25] MnO_2 particles were observed to have been developed on the surface and surrounding UiO-66, exhibiting a relatively dense distribution. To confirm the identity of the particulates present on the surface as UiO-66 and MnO_2, Fig. 4c presents the EDX spectrum of the crystal of H-UiO-66, which, in conjunction with the UiO-66 components, further validates the Mn presence resulting from the Hummers' method.[26] The poorly crystallized amorphous phase is anticipated to exhibit higher specific capacitance compared to the crystalline phase. This expectation arises from the unorganized

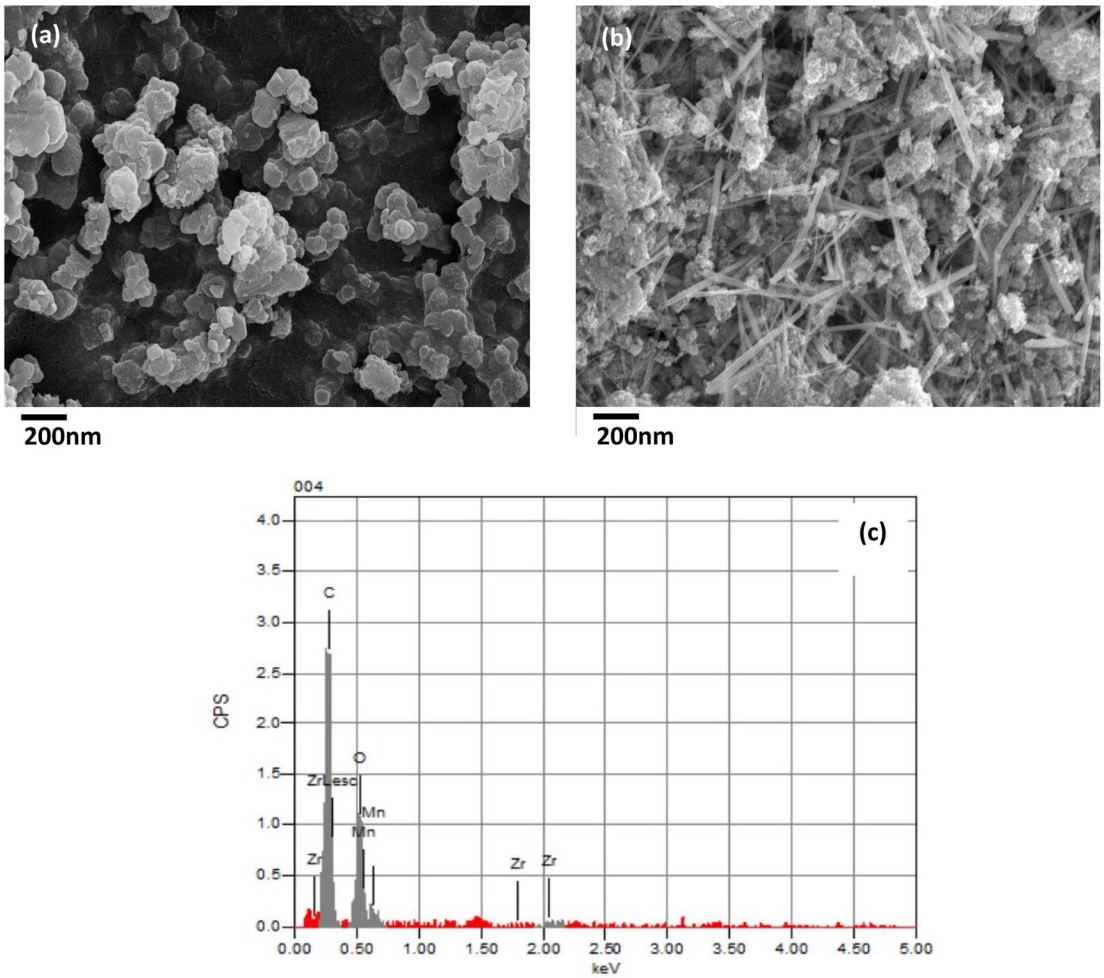

Fig. 4 SEM images of UiO-66 (a), H-UiO-66 (b), and EDX spectra of H-UiO-66 (c).

 © 2025 The Author(s). Published by the Royal Society of Chemistry

Open Access Article. Published on 10 January 2025. Downloaded on 1/22/2026 12:59:05 AM.
This article is licensed under a Creative Commons Attribution-NonCommercial 3.0 Unported Licence.

internal structure of the amorphous phase, which is linked to increased reactivity and a higher density of active sites.[27] Additionally, the conductivity is improving from graphitization.

The XPS analysis was utilized to further confirm the chemical composition and bonding state of H-UiO-66 and UiO-66, as shown in Fig. 5. The XPS spectrum of H-UiO-66 Fig. 5a shows Zr, O, Mn, and C elements. However, Fig. 5b exhibits XPS spectrum peaks of C 1s at 284.5 and 286.2 eV, corresponding to sp^2 carbon and epoxide ring, respectively.[28] The π–π* shake-up G interactions are observed at 291.8 and 294.5 eV for H-UiO-66, and are characteristic of conjugated systems or aromatic groups.[29] The binding energies of Zr $3d_{3/2}$ and Zr $3d_{5/2}$ were recorded as 185.1 and 182.7 eV, respectively, without using Hummer's methods. However, after applying Hummer's methods, these peaks

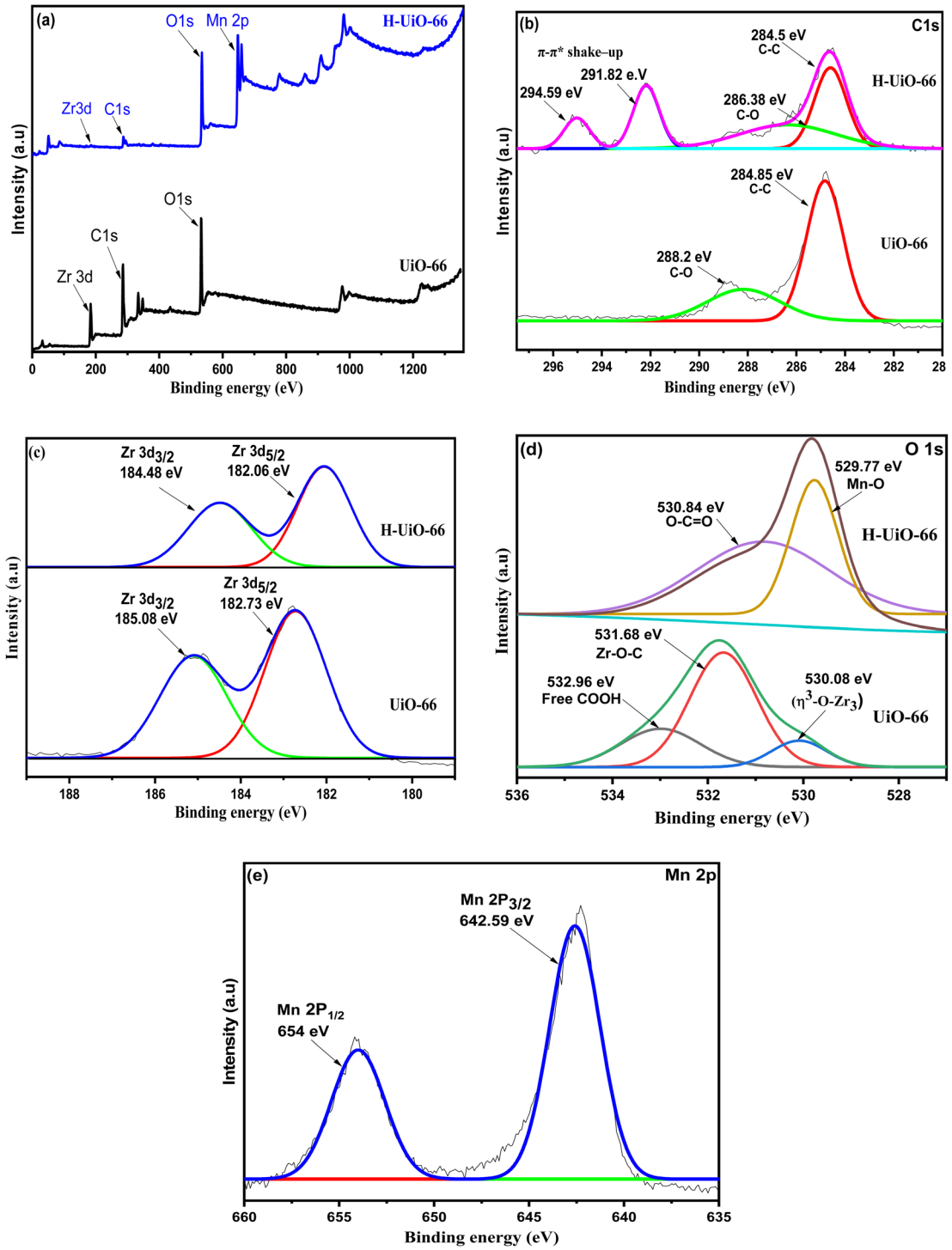

Fig. 5 XPS analysis of UiO-66 and H-UiO-66: (a) survey spectra of elements and XPS spectra high resolution of C 1s (b), Zr 2d (c), O 1s (d), and Mn 2p (e).

Open Access Article. Published on 10 January 2025. Downloaded on 1/22/2026 12:59:05 AM.
This article is licensed under a Creative Commons Attribution-NonCommercial 3.0 Unported Licence.

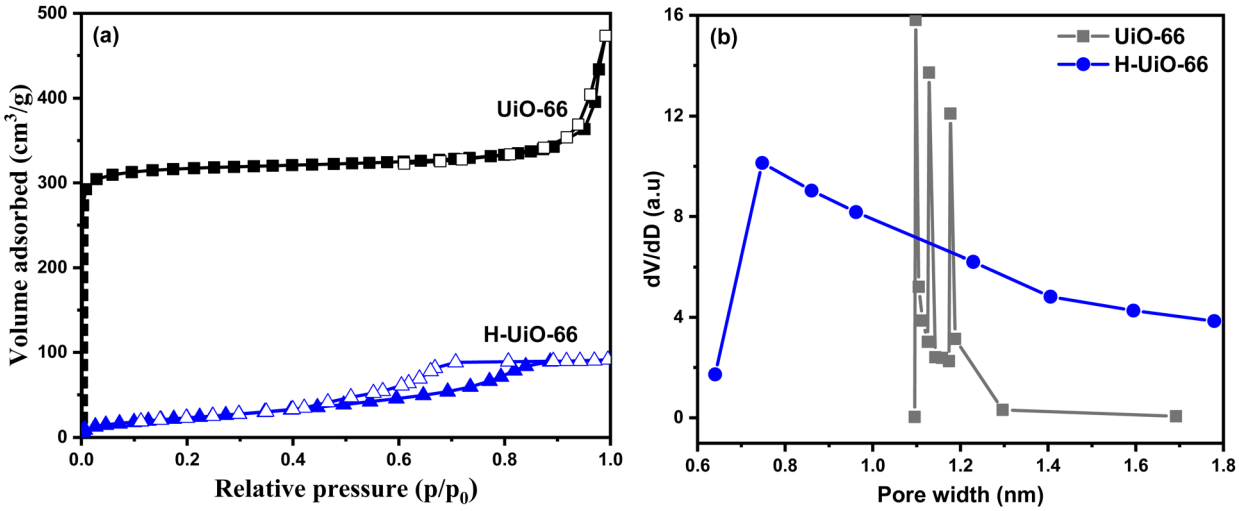

Fig. 6 N_2 sorption isotherm (a) and pore size distribution (b) of UiO-66 and H-UiO-66 samples.

showed a shift of 0.6 eV. As a result, the new values for Zr $3d_{3/2}$ and Zr $3d_{5/2}$ are 184.5 eV and 182.1 eV, respectively (Fig. 5c). This suggested that the chemical bonding environmental change around the Zr-cluster was due to the deterioration of the framework *via* oxidation and the formation of the more electronegative Mn–O bonds.[26] From XPS spectra high-resolution of O 1s (Fig. 5g), the peak observed at 529.7 eV corresponded to the bond of Mn–O of MnO_2. Furthermore, the observed peak at 531.2 eV was assigned to the Zr–OH bond. The findings indicated that the recombination of H-UiO-66 was successful.

Fig. 6 provides a nitrogen sorption isotherm and pore size distribution graphs comparing two substances, UiO-66 and H-UiO-66. The graph shows two distinct curves for each substance, with the data points for UiO-66 shown in black and the data points for H-UiO-66 shown in blue. For UiO-66, the nitrogen sorption isotherm curve exhibits a Type I isotherm behavior (Fig. 6a). This indicates a material with microporous characteristics, typically associated with materials having a high surface area and pore volume (1150 $m^2\ g^{-1}$ and 0.61 $cm^3\ g^{-1}$). The steep increase in adsorbed volume at low relative pressures suggests a well-defined pore structure with high accessibility to nitrogen molecules.[30,31] On the other hand, the nitrogen sorption isotherm curve for H-UiO-66 shows a Type IV isotherm behavior with lower surface area and pore volume (87 $m^2\ g^{-1}$ and 0.14 $cm^3\ g^{-1}$) due to the deterioration of the framework *via* oxidation. This isotherm type is typical of mesoporous materials with diverse pore sizes. The initial gradual uptake of nitrogen followed by a sharper increase at higher relative pressures suggests the presence of larger mesopores within the material (Fig. 6a). Additionally, Fig. 6b show the pore size distribution and confirm the microporosity of both samples. In summary, UiO-66 exhibits a microporous nature with a Type I isotherm, while H-UiO-66 displays a mesoporous nature with a Type IV isotherm. These findings provide insights into the porosity and pore size distribution of the two substances.

The thermal analysis of UiO-66 and H-UiO-66, as shown in Fig. 7, reveals distinct decomposition profiles that reflect their structural stability and compositional differences. For UiO-66, the TGA curve indicates a three-step weight loss: the initial loss (~12.48%) below 150 °C corresponds to the removal of adsorbed moisture or residual solvents.[32,33] The subsequent weight losses (~10.06% and ~23.75%) represent the

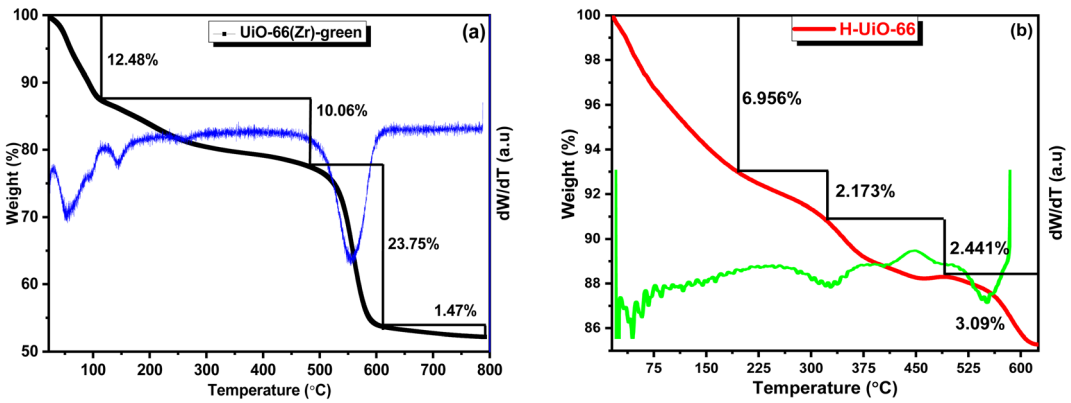

Fig. 7 TGA and DTA curves of UiO-66 (a) and H-UiO-66 (b) samples.

 © 2025 The Author(s). Published by the Royal Society of Chemistry

Open Access Article. Published on 10 January 2025. Downloaded on 1/22/2026 12:59:05 AM.
This article is licensed under a Creative Commons Attribution-NonCommercial 3.0 Unported Licence.

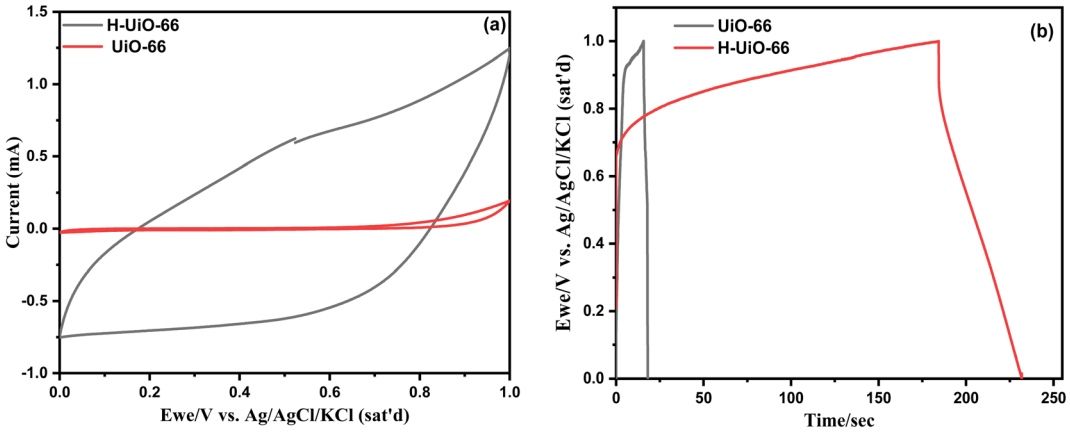

Fig. 8 (a) CV curves of H-UiO-66 and UiO-66 samples at the scan rate of 10 mV s^{-1}, (b) GCD curves of UiO-66 and H-UiO-66 samples at the current of 1 mA.

decomposition of organic linkers and the framework collapse around 500–600 °C.[34,35] H-UiO-66, modified by Hummers' method, exhibits smaller weight losses (∼6.95%, ∼2.17%, ∼2.44%, and ∼3.09%) at corresponding temperature ranges, indicating reduced solvent retention and a potentially more defect-rich structure (Fig. 7b). These changes reflect the introduction of oxidative modifications, which slightly lower the thermal stability of H-UiO-66 compared to UiO-66, while maintaining significant resilience under heat. The derivative curves (dW/dT) confirm distinct decomposition events for each material, highlighting their structural transformations.

3.2. Electrochemical performance test

Measurements of electrochemical properties, such as galvanostatic charge and discharge (GCD), cyclic voltammetry (CV), and electrochemical impedance spectroscopy (EIS), utilizing a three-electrode configuration in a 0.5 M Na_2SO_4 aqueous electrolyte. The active substance electrode on the stainless-steel piece serves to be the applied electrode, the Ag/AgCl electrode (KCl Sat.) is the electrode of reference, and the wire of platinum electrode is the electrode of counter.

3.2.1. Electrochemical properties. First, the electrochemical behaviors of H-UiO-66 and UiO-66 were discussed. Fig. 8a illustrates the CV curves of two samples of H-UiO-66 and UiO-66, which display semi-rectangles at a rate of scan of 10 mV s^{-1}, primarily indicating electric double layer characteristics (EDLC). The CV curve of UiO-66 shows the smallest looping area, indicating a lower specific capacitance attributed to its poor conductivity. Nevertheless, H-UiO-66 demonstrates the most extensive looping area, indicating the greatest specific capacitance. In Fig. 8b, the GCD curves display the data at the actual applied current of 1 mA, and The H-UiO-66 demonstrates the longest discharge duration, aligning with the highest specific capacity observed, which is corroborated by the CV results. The specific capacitance of the H-UiO-66 has been calculated to be as high as 82.8 F g^{-1}, which is significantly greater than that of the UiO-66 (0.18 F g^{-1}) because of the graphitization of UiO-66. The result reveals the conductivity enhancement of UiO-66 when an electroactive process is performed for supercapacitors by the graphitization method (Hummer's approach).

Fig. 9, The curves of GCD and CV of H-UiO-66 at several densities of current and scanning rates are presented. With the

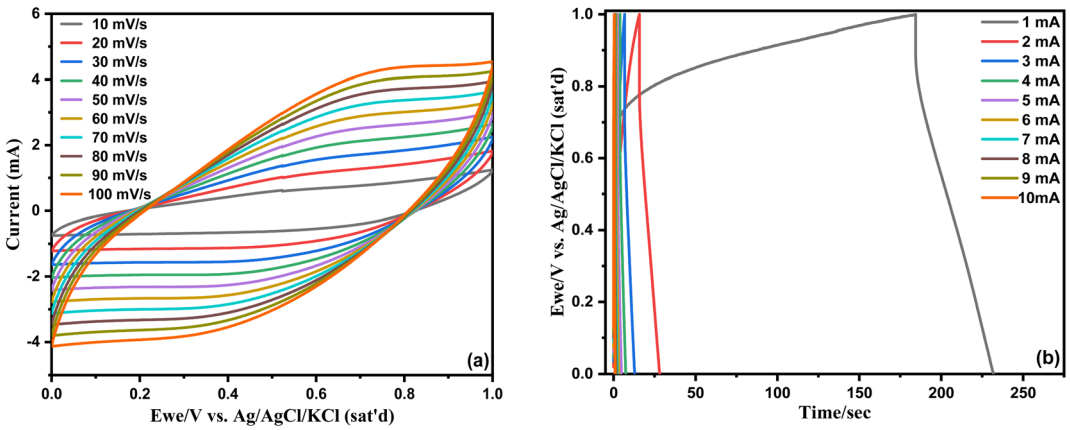

Fig. 9 (a) CV measurement for H-UiO-66 electrode at various scan rates, (b) GCD curve for H-UiO-66 electrode for different currents.

Open Access Article. Published on 10 January 2025. Downloaded on 1/22/2026 12:59:05 AM.
This article is licensed under a Creative Commons Attribution-NonCommercial 3.0 Unported Licence.

increase in the rate of scan from 10 to 100 mV s^{-1}, The curves of CV exhibit notable deformation, and the areas delineated by the curves of CV progressively expand, and the defined area of the CV curves is progressively increasing, This is an impressive (EDLC) characteristic of SCs. The outcome is primarily attributed to insufficient interaction between the electrolyte and electrode, along with a more pronounced effect of polarization.[36] Furthermore, as the current is adjusted to 2 mA, a specific capacitance of 45.4 F g^{-1} is obtained, Approximately 54% of the initial capacitance at 1 mA (82.8 F g^{-1}). The primary factor contributing to the reduction in the specific capacitance is that the ions of the electrolyte lack sufficient time for diffusion into the surface of the electrode, particularly under high currents.[37] In short, they demonstrate remarkable rate capability.

As shown in Fig. 10a, with the increase in the actual current, the specific capacitances of H-UiO-66 exhibit a decreasing pattern. Typically, the electrochemical efficiency of H-UiO-66 is markedly superior to that of UiO-66 due to the conductivity enhancement and MnO_2 incorporation during graphitization by Hummer's method. Specifically, the sample of H-UiO-66 exhibits the highest observed specific capacitance. In Fig. 10c, it's important to note that the H-UiO-66 specific capacitance did not decrease through 2000 cycles but increased, which can be seen from the increased ratio of the specific capacitance of H-UiO-66. During the initial 100 cycles, the significant rise in capacitance is linked to the electro-activation of the electrode material and the electrochemical reduction of the H-UiO-66. During the second phase, which spans from 100 to 2000 cycles, there is a consistent increase in capacitance. This trend may be attributed to the exhaustion of oxygenated groups on the electrode surface as the reduction of H-UiO-66 advances.[38] Additionally, The coulombic efficiency of H-UiO-66 is consistently higher than that of UiO-66 across the current range (Fig. 10d), indicating superior charge transfer and electrochemical performance for H-UiO-66. H-UiO-66 achieves near 100% efficiency at low currents (2–5 mA), maintaining stability, while UiO-66 shows lower efficiency, peaking at around 50%, with significant fluctuations. This suggests that the modifications introduced in H-UiO-66 enhance its electrochemical properties, likely due to structural defects or improved conductivity from the Hummers' method.

The observed plot in Fig. 11 indicates varying behaviors across the used frequency range, with the high-frequency area characterized by a half circle and the low-frequency area characterized by a linear representation. This indicates the presence of both capacitive and resistive characteristics of the examined electrode. It is evident that at the high-frequency area, one of

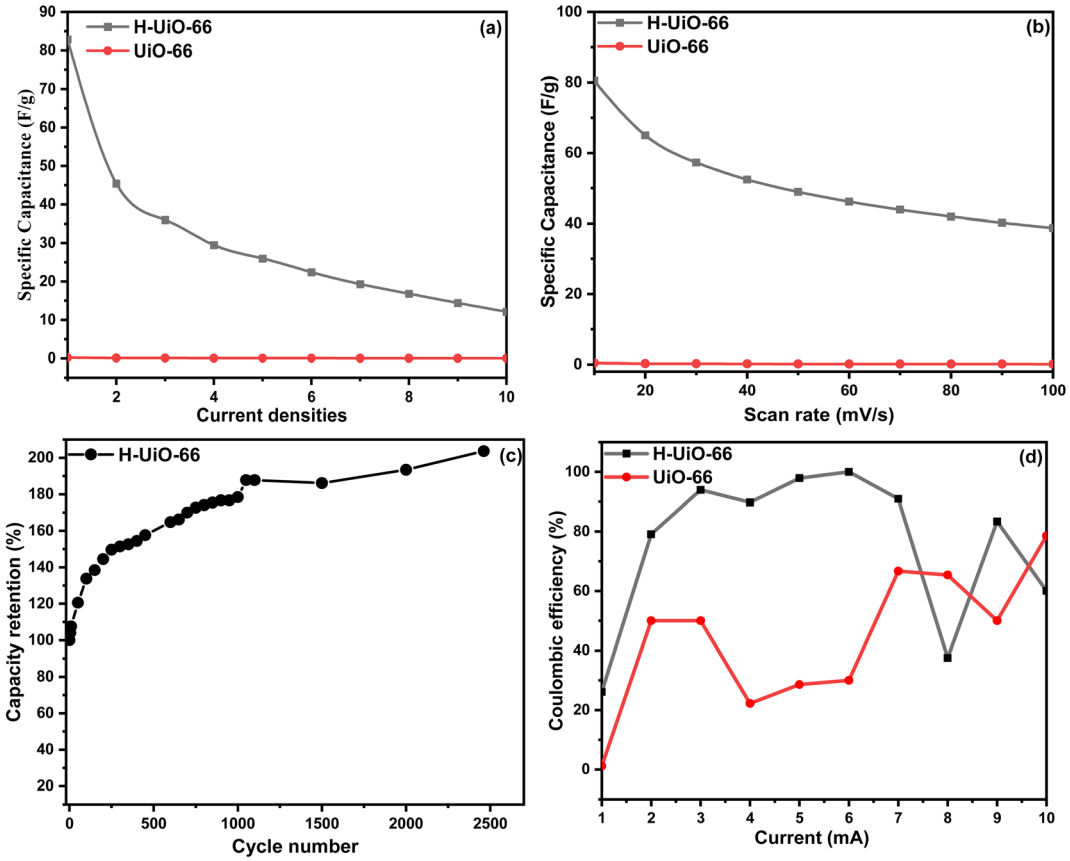

Fig. 10 (a) Specific capacitance of H-UiO-66 and UiO-66 samples at different current densities, (b) the UiO-66 and H-UiO-66 specific capacitance as several scan rates, (c) UiO-66 specific capacitance percentage of H-UiO-66 for cycling performance at an actual current of 3 mA, and (d) the coulombic efficiency of UiO-66 and H-UiO-66.

 © 2025 The Author(s). Published by the Royal Society of Chemistry

Open Access Article. Published on 10 January 2025. Downloaded on 1/22/2026 12:59:05 AM.
This article is licensed under a Creative Commons Attribution-NonCommercial 3.0 Unported Licence.

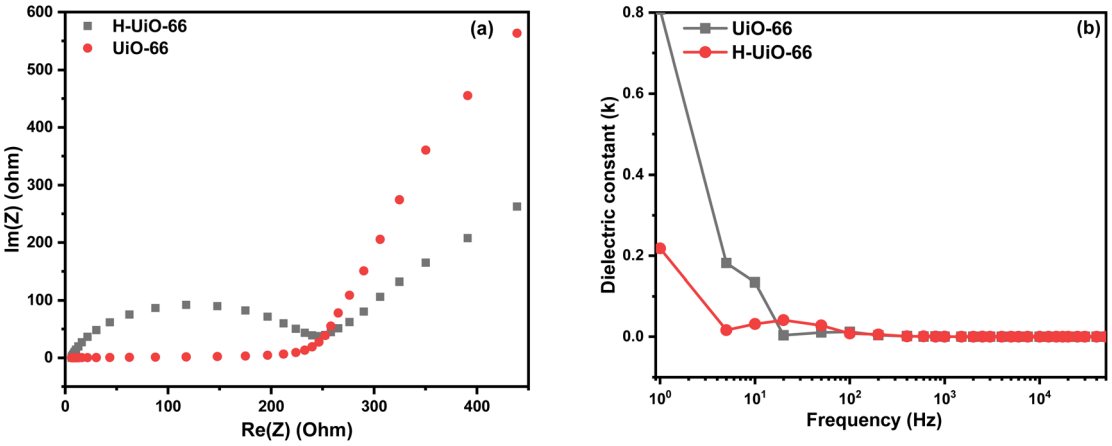

Fig. 11 EIS spectra (a) and dielectric constant (b) of UiO-66 and H-UiO-66 samples.

the samples shows an ideal arc, which corresponds to the resistance of charge transfer (R_{ct}) (262.6 ohm). Furthermore, the minimal x-axis intercept indicates that the electrode material internal resistance (R_s) is very low at 5.65 ohm, which may present a nearly optimal capacitive response for the electrolyte-filled pores ionic resistance within the electrode.[39] An almost perpendicular line indicates reduced resistance of ion diffusion (R_w) of electrolytes, demonstrating a well-capacitive action in the low-frequency area.[36] According to the Fig. 11b, UiO-66 exhibits a higher dielectric constant compared to H-UiO-66 at lower frequencies, suggesting a greater ability to store charge. However, as frequency increases, both materials converge to similar values, indicating comparable dielectric behavior at higher frequencies. Since a higher dielectric constant is often associated with lower conductivity (due to better charge storage and less dissipation), H-UiO-66, with its consistently lower dielectric constant across frequencies, is likely more conductive than UiO-66. This aligns with the modification introduced by Hummers' method, which typically enhances conductive properties by graphitization and introducing functional groups that facilitate charge transport.

Table 1 provides a comparison of the electrochemical properties from the specific capacitance (F g^{-1}), of H-UiO-66 and UiO-66 with other UiO-66-based materials reported in the literature. In comparison, the H-UiO-6 in our study demonstrates a specific capacitance of 82.8 F g^{-1} at 0.14 A g^{-1}, which still shows promising energy storage applications. On the other hand, UiO-66 without modifications shows a substantially lower capacitance of 0.18 F g^{-1} at 0.19 A g^{-1}, highlighting the need for further enhancements to its electrochemical properties as compared with other reported work in the literature. Overall, the comparison shows that modifications, including composite formation and structural changes, can significantly improve the electrochemical performance of UiO-66, making it more suitable for applications in supercapacitors and other energy storage devices.

Table 1 Electrochemical properties of some reported electrodes based on UiO-66

Active material	Measured condition	C_f (F g^{-1})	Ref.
C-UiO-66	1 A g^{-1}	32.78	1
C-UiO-66-AT	1 A g^{-1}	117.7	1
PI/5%UiO-66–800	0.5 A g^{-1}	271.2	36
HP-UiO-66	0.5 A g^{-1}	90.0	36
Amorphous UiO-66	0.8 A g^{-1}	610	6
PEDOT/UiO66-NH_2	0.5 A g^{-1}	293	40
UiO-66/ZrO_2	1 A g^{-1}	913.8	41
H-UiO-66	**0.14 A g^{-1}**	**82.8**	**This work**
UiO-66	**0.19 A g^{-1}**	**0.18**	**This work**

4 Conclusion

In this study, the potential of UiO-66, a zirconium-based metal–organic framework (MOF), as a material of electrode for SCs, was explored. The primary challenge of UiO-66's poor electrical conductivity was addressed by employing the Hummers' method to oxidize the organic linker of UiO-66, resulting in a material referred to as H-UiO-66. Comprehensive characterization using (XRD), (SEM), (FTIR), (XPS), and (BET) analysis confirmed the successful graphitization of UiO-66. The electrochemical performance of H-UiO-66 was significantly improved compared to pristine UiO-66, as evidenced (CV), (GCD), and (EIS) measurements. H-UiO-66 exhibited a remarkable specific capacitance of 82.8 F g^{-1} at a current of 1 mA, far surpassing the 0.18 F g^{-1} of the original UiO-66. This substantial enhancement is attributed to the increased conductivity and electrochemical activity achieved through the graphitization process *via* Hummer's method. The findings of this study demonstrate that the Hummers' method is an effective strategy for improving the electrical conductivity and overall performance of UiO-66 in supercapacitor applications. The enhanced properties of H-UiO-66 make it a promising candidate for use in high-performance supercapacitors, bridging the gap between traditional capacitors and batteries. Future research could focus on further optimizing the synthesis process and exploring other conductive matrices to integrate with UiO-66, aiming to improve efficiency in energy storage devices.

Open Access Article. Published on 10 January 2025. Downloaded on 1/22/2026 12:59:05 AM.
This article is licensed under a Creative Commons Attribution-NonCommercial 3.0 Unported Licence.

Data availability

All data generated or analyzed during this study are included in this manuscript file.

Conflicts of interest

There are no conflicts to declare.

Acknowledgements

The authors are most grateful for the technical support provided by the Labs of the Physics and Chemistry Departments, Faculty of Science, Menoufia University, Egypt, and for the funding provided by the Post-doctoral Foundation Project of Shenzhen Polytechnic University (no. 6024331007K).

References

1 Y.-S. Sung and L.-Y. Lin, Improving energy storage ability of Universitetet i Oslo-66 as active material of supercapacitor using carbonization and acid treatment, *J. Energy Storage*, 2021, **37**, 102480.

2 M. Safaei, M. M. Foroughi, N. Ebrahimpoor, S. Jahani, A. Omidi and M. Khatami, A review on metal-organic frameworks: Synthesis and applications, *TrAC, Trends Anal. Chem.*, 2019, **118**, 401–425.

3 C. Zhang, J. Tian, W. Rao, B. Guo, L. Fan, W. Xu and J. Xu, Polypyrrole@ metal-organic framework (UiO-66)@cotton fabric electrodes for flexible supercapacitors, *Cellulose*, 2019, **26**, 3387–3399.

4 Y. Wang, L. Wang, W. Huang, T. Zhang, X. Hu, J. A. Perman and S. Ma, A metal–organic framework and conducting polymer based electrochemical sensor for high performance cadmium ion detection, *J. Mater. Chem. A*, 2017, **5**(18), 8385–8393.

5 L. Shao, Q. Wang, Z. Ma, Z. Ji, X. Wang, D. Song, *et al.*, A high-capacitance flexible solid-state supercapacitor based on polyaniline and Metal-Organic Framework (UiO-66) composites, *J. Power Sources*, 2018, **379**, 350–361.

6 F. Yang, W. Li and B. Tang, Facile synthesis of amorphous UiO-66 (Zr-MOF) for supercapacitor application, *J. Alloys Compd.*, 2018, **733**, 8–14.

7 W. Gao, D. Chen, H. Quan, R. Zou, W. Wang, X. Luo and L. Guo, Fabrication of hierarchical porous metal–organic framework electrode for aqueous asymmetric supercapacitor, *ACS Sustain. Chem. Eng.*, 2017, **5**(5), 4144–4153.

8 Y. Tan, W. Zhang, Y. Gao, J. Wu and B. Tang, Facile synthesis and supercapacitive properties of Zr-metal organic frameworks (UiO-66), *RSC Adv.*, 2015, **5**(23), 17601–17605.

9 Y. Guo, J. Tang, R. R. Salunkhe, Z. A. Alothman, M. S. A. Hossain, V. Malgras and Y. Yamauchi, Effect of various carbonization temperatures on ZIF-67 derived nanoporous carbons, *Bull. Chem. Soc. Jpn.*, 2017, **90**(8), 939–942.

10 J. Zhang, Y. Wang, K. Xiao, S. Cheng, T. Zhang, G. Qian, *et al.*, N-Doped hierarchically porous carbon derived from heterogeneous core–shell ZIF-L(Zn)@ZIF-67 for supercapacitor application, *New J. Chem.*, 2018, **42**(9), 6719–6726.

11 J. Xu, C. Xu, Y. Zhao, J. Wu and J. Hu, Hollow Co_3O_4@MnO_2 cubic derived from ZIF-67@ Mn-ZIF as electrode materials for supercapacitors, *Front. Chem.*, 2019, **7**, 831.

12 Y. Miao, Y. Sui, D. Zhang, J. Qi, F. Wei, Q. Meng, *et al.*, Polyhedral $NiCoSe_2$ synthesized *via* selenization of metal-organic framework for supercapacitors, *Mater. Lett.*, 2019, **242**, 42–46.

13 G. Qu, X. Zhang, G. Xiang, Y. Wei, J. Yin, Z. Wang, *et al.*, ZIF-67 derived hollow Ni-Co-Se nano-polyhedrons for flexible hybrid supercapacitors with remarkable electrochemical performances, *Chin. Chem. Lett.*, 2020, **31**(7), 2007–2012.

14 A. S. Abou-Elyazed, G. Ye, Y. Sun and A. M. El-Nahas, A Series of UiO-66(Zr)-Structured Materials with Defects as Heterogeneous Catalysts for Biodiesel Production, *Ind. Eng. Chem. Res.*, 2019, **58**(48), 21961–21971.

15 M. P. Lavin-Lopez, A. Romero, J. Garrido, L. Sanchez-Silva and J. L. Valverde, Influence of Different Improved Hummers Method Modifications on the Characteristics of Graphite Oxide in Order to Make a More Easily Scalable Method, *Ind. Eng. Chem. Res.*, 2016, **55**(50), 12836–12847.

16 G. Zhang, F. Liu, Y. Qu, Y. Zheng, Y. Cao, F. Liu, *et al.*, Controllable creating mesoporous coordination unsaturated sites in UiO-66 single crystals for efficient conversion of hydrogen sulfide into polysulphur, *Chem. Eng. J.*, 2024, **479**, 147565.

17 R. Al-Gaashani, A. Najjar, Y. Zakaria, S. Mansour and M. Atieh, XPS and structural studies of high quality graphene oxide and reduced graphene oxide prepared by different chemical oxidation methods, *Ceram. Int.*, 2019, **45**(11), 14439–14448.

18 V. Sannasi and K. Subbian, Influence of Moringa oleifera gum on two polymorphs synthesis of MnO2 and evaluation of the pseudo-capacitance activity, *J. Mater. Sci.: Mater. Electron.*, 2020, **31**(19), 17120–17132.

19 X. Jiang, S. Li, S. He, Y. Bai and L. Shao, Interface manipulation of CO_2–philic composite membranes containing designed UiO-66 derivatives towards highly efficient CO_2 capture, *J. Mater. Chem. A*, 2018, **6**(31), 15064–15073.

20 M. A. Rodrigues, J. d. S. Ribeiro, E. d. S. Costa, J. L. d. Miranda and H. C. Ferraz, Nanostructured membranes containing UiO-66(Zr) and MIL-101(Cr) for O_2/N_2 and CO_2/N_2 separation, *Sep. Purif. Technol.*, 2018, **192**, 491–500.

21 M. Bahmani, D. Mowla, F. Esmaeilzadeh and M. Ghaedi, $BiFeO_3$–BiOI impregnation to UiO-66(Zr/Ti) as a promising candidate visible-light-driven photocatalyst for boosting urea photodecomposition in a continuous flow-loop thin-film slurry flat-plate photoreactor, *J. Solid State Chem.*, 2020, **286**, 121304.

22 J. Wei, Y. Chen, H. Zhang, Z. Zhuang and Y. Yu, Hierarchically porous S-scheme CdS/UiO-66 photocatalyst

 © 2025 The Author(s). Published by the Royal Society of Chemistry

Open Access Article. Published on 10 January 2025. Downloaded on 1/22/2026 12:59:05 AM.
This article is licensed under a Creative Commons Attribution-NonCommercial 3.0 Unported Licence.

for efficient 4-nitroaniline reduction, *Chin. J. Catal.*, 2021, **42**(1), 78–86.

23 D. He, Z. Peng, W. Gong, Y. Luo, P. Zhao and L. Kong, Mechanism of a green graphene oxide reduction with reusable potassium carbonate, *RSC Adv.*, 2015, **5**(16), 11966–11972.

24 J. Chu, D. Lu, J. Ma, M. Wang, X. Wang and S. Xiong, Controlled growth of MnO_2 *via* a facile one-step hydrothermal method and their application in supercapacitors, *Mater. Lett.*, 2017, **193**, 263–275.

25 H. Liu, J. Liu, Z. Yang and D. Tang, Controlled construction of hierarchical hollow micro/nano urchin-like β-MnO_2 with superior lithium storage performance, *J. Alloys Compd.*, 2019, **795**, 336–342.

26 Y. Zhou, S. Feng, X. Duan, W. Zheng, C. Shao, W. Wu, *et al.*, MnO_2/UiO-66 improves the catalysed degradation of oxytetracycline under UV/H_2O_2/PMS system, *J. Solid State Chem.*, 2021, **300**, 122231.

27 T. Guan, X. Li, W. Fang and D. Wu, Efficient removal of phosphate from acidified urine using UiO-66 metal-organic frameworks with varying functional groups, *Appl. Surf. Sci.*, 2020, **501**, 144074.

28 F. T. Johra, J.-W. Lee and W.-G. Jung, Facile and safe graphene preparation on solution based platform, *J. Ind. Eng. Chem.*, 2014, **20**(5), 2883–2887.

29 J. Indujalekshmi, P. Krishnan, R. V. Reji and V. Biju, L-ascorbic acid-reduced graphite oxide as active material for supercapacitors, *Mater. Today: Proc.*, 2023, **2**, 159.

30 A. S. Abou-Elyazed, G. Ye, Y. Sun and A. M. El-Nahas, A series of UiO-66 (Zr)-structured materials with defects as heterogeneous catalysts for biodiesel production, *Ind. Eng. Chem. Res.*, 2019, **58**(48), 21961–21971.

31 A. Abou-Elyazed, Y. Sun, A. El-Nahas, S. Abdel-Azeim, T. Sharara and A. Yousif, Solvent-free synthesis and characterization of Ca^{2+}-doped UiO-66 (Zr) as heterogeneous catalyst for esterification of oleic acid with methanol: a joint experimental and computational study, *Mater. Today Sustain.*, 2022, **18**, 100110.

32 A. S. Abou-Elyazed, E. A. Shaban, Y. Sun, A. M. El-Nahas and T. I. Kashar, Solvent-free synthesis and characterization of bimetallic UiO-66(Zr/Sn) heterogeneous catalyst for biodiesel production, *Ind. Eng. Chem. Res.*, 2023, **62**(23), 9211–9220.

33 A. S. Abou-Elyazed, Y. Sun, A. M. El-Nahas and A. M. Yousif, A green approach for enhancing the hydrophobicity of UiO-66 (Zr) catalysts for biodiesel production at 298 K, *RSC Adv.*, 2020, **10**(68), 41283–41295.

34 Q. Yang, H.-Y. Zhang, L. Wang, Y. Zhang and J. Zhao, Ru/UiO-66 Catalyst for the Reduction of Nitroarenes and Tandem Reaction of Alcohol Oxidation/Knoevenagel Condensation, *ACS Omega*, 2018, **3**(4), 4199–4212.

35 J. Farrando-Pérez, G. Martinez-Navarrete, J. Gandara-Loe, S. Reljic, A. Garcia-Ripoll, E. Fernandez and J. Silvestre-Albero, Controlling the Adsorption and Release of Ocular Drugs in Metal–Organic Frameworks: Effect of Polar Functional Groups, *Inorg. Chem.*, 2022, **61**(47), 18861–18872.

36 Y. Wang, Y. Lu, Z. Hu, J. Sun, G. Xiao, H. Zhao, *et al.*, Facile preparation of Zr@carbon electrodes based on polyimide/UiO-66 composites for supercapacitors, *Electrochem. Commun.*, 2023, **148**, 107449.

37 H. Peng, S. Qi, Q. Miao, R. Zhao, Y. Xu, G. Ma and Z. Lei, Formation of nitrogen-doped holey carbon nanosheets *via* self-generated template assisted carbonization of polyimide nanoflowers for supercapacitor, *J. Power Sources*, 2021, **482**, 228993.

38 S. H. Aboutalebi, A. T. Chidembo, M. Salari, K. Konstantinov, D. Wexler, H. K. Liu and S. X. Dou, Comparison of GO, GO/MWCNTs composite and MWCNTs as potential electrode materials for supercapacitors, *Energy Environ. Sci.*, 2011, **4**(5), 1855–1865.

39 Y. Wang, Y. Lu, X. Liu, H. Chi, J. Hu, H. Zhao and G. Xiao, Facile synthesis and electrochemical properties of alicyclic polyimides based carbon microflowers for electrode materials of supercapacitors, *J. Energy Storage*, 2022, **47**, 103656.

40 W. Sharmoukh, Z. M. Hassan, S. G. Mohamed and H. N. Abdelhamid, Metal-organic frameworks (UiO66-NH2)/PEDOT-derived ZrO_2/N, S-doped carbon for supercapacitors, *J. Energy Storage*, 2024, **102**, 114071.

41 R. M. Nageib, A. A. El Amin, R. M. Salm, M. Gaber and S. G. Mohamed, Simultaneous synthesis of UiO-66/ZrO_2 composites for high-performance supercapacitors: Fabrication, characterization, and electrochemical evaluation, *J. Energy Storage*, 2024, **91**, 112047.